Multiscale Digital Porous Rock Reconstruction Using Template Matching

W. Lin[1,2,3], X. Li[1,3], Z. Yang[1,3], M. Manga[2], X. Fu[2], S. Xiong[1,3], A. Gong[4], G. Chen[4], H. Li[4], L. Pei[4], S. Li[4], X. Zhao[1,3], and X. Wang[3]

[1] Institute of Porous Flow and Fluid Mechanics, University of Chinese Academy of Sciences, Langfang, China, [2] Department of Earth and Planetary Science, University of California, Berkeley, CA, USA, [3] College of Computer and Communication Engineering, China University of Petroleum (East China), Qingdao, China, [4] Research Institute of Petroleum Exploration and Development, PetroChina Company Limited, Beijing, China

Correspondence to: M. Manga, manga@seismo.berkeley.edu

Abstract

Rocks are heterogeneous multiscale porous media: two rock samples with identical bulk properties can vary widely in microstructure. The advent of digital rock technology and modern 3-D printing provides new opportunities to replicate rocks. However, the inherent trade-off between imaging resolution and sample size limits the scales over which microstructure and macrostructure can be identified and related to each other. Here, we develop a multiscale digital rock construction strategy by combining X-ray computed microtomography and focused-ion beam (FIB)-scanning electron microscope (SEM) images, and we apply the technique to a tight sandstone. The computed tomography (CT) scanning images characterize macroscale pore structures, while the FIB-SEM images capture microscale pore textures. The FIB-SEM images are then coupled to CT images via a template-matching algorithm and superposition. Bulk properties, including porosity and pore and throat size distribution, can be recovered with this approach. Permeability prediction with a pore network model for the largest connected pore network are 3 orders and 1 order of magnitude greater than the bulk rock measured value using the CT-only and the SEM-CT coupled images, respectively.

1 Introduction

Digital rock models offer many opportunities to study flow and transport processes in geomaterials such as rocks and soils, either through numerical simulation (e.g., digitalrocksportal.org) or through 3-D printing of models for experimentation (e.g., as reviewed in Hwa et al., 2017; Ishutov et al., 2018; Jiang et al., 2016). Most natural geomaterials, however, contain multiscale pore structures, with dimensions ranging from the nanometer to the sample scale. As a consequence, the full range of spatial scales can be challenging to image or characterize and hence to be captured in digital rock models.

There is a fundamental challenge from the trade-off between resolution and dimension, which limits the ability to simultaneously capture macroscale features of rocks, characterize heterogeneity, and resolve fine pore-throat structures. Efforts to overcome this challenge include using different and

complementary methods to image (e.g., Ma et al., 2017; Sok et al., 2010), characterize (e.g., Wu et al., 2017), or simulate flow and transport (e.g., Wang et al., 2017) over a range of scales.

Here we explore a technique for multiscale digital rock reconstruction to assess its promise. We construct digital rocks from images taken at two different spatial resolutions that preserve spatial correlations between the macroscale and the microscale. The macropores are imaged with computed tomography (CT). The micro pores of the same sample are imaged using a focused-ion beam (FIB)-scanning electron microscope (SEM). We then introduce a template-matching algorithm (also called patch-based algorithm) and local resolution improvement to create multiscale digital rock. Figure 1 summarizes the steps in the analysis. We show that bulk rock properties such as porosity, pore size, and throat size distributions can be captured with the approach. Computed permeabilities using a pore network model extracted from the hybrid images are improved but still deviate from experimental measurements of the sample tight sandstone.

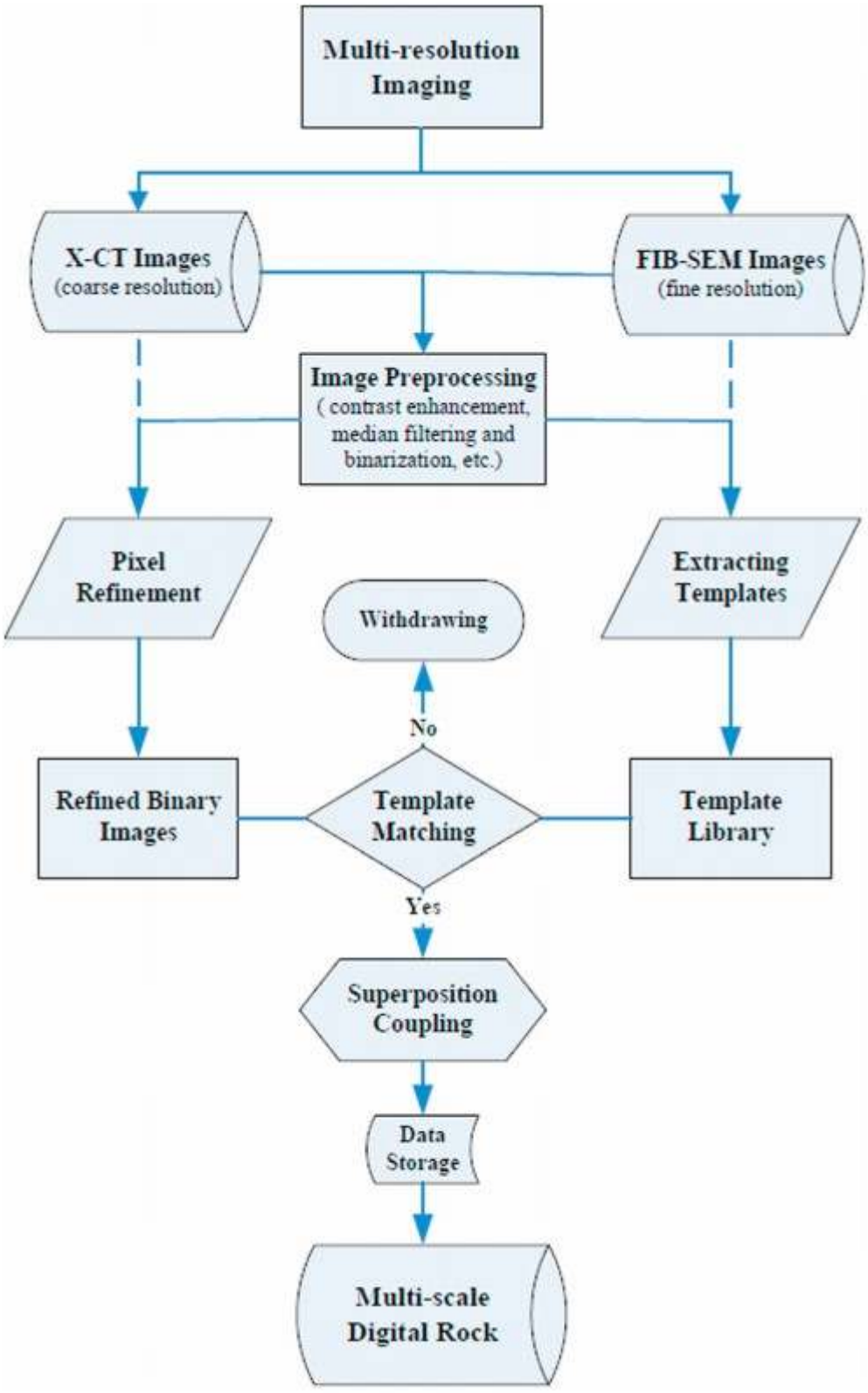

Figure 1. Flowchart for multiscale digital porous rock reconstruction using template matching. CT = computed tomography; FIB = focused-ion beam; SEM = scanning electron microscope.

2 Samples and Experimental Procedures

As a test case, we characterize a sandstone sample from the fourth member of Quantou Formation, southern Songliao Basin, Jilin oilfield, China. These sandstones are tight rocks that contain primary and secondary pores. The primary pores have straight edges, clean pore interiors, and large pore radii. The secondary pores mainly include intragranular and marginal pores of feldspar and detritus, a small number of dissolved pores in carbonate cements, and intercrystalline pores in clay minerals. Figure 2 shows the geometry of the void space in this tight sandstone sample. The sample contains macropores, micropores and throats, and the void size distribution range is large. In Figure 2, the structures marked by two arrows are fine throats extending along the plane, the structures marked by three arrows are throats extending normal to the imaged surface or are micropores, and the region highlighted by the dashed circle is the corner of a macropore. These highlighted features are usually identified as being solid in coarse-resolution imaging.

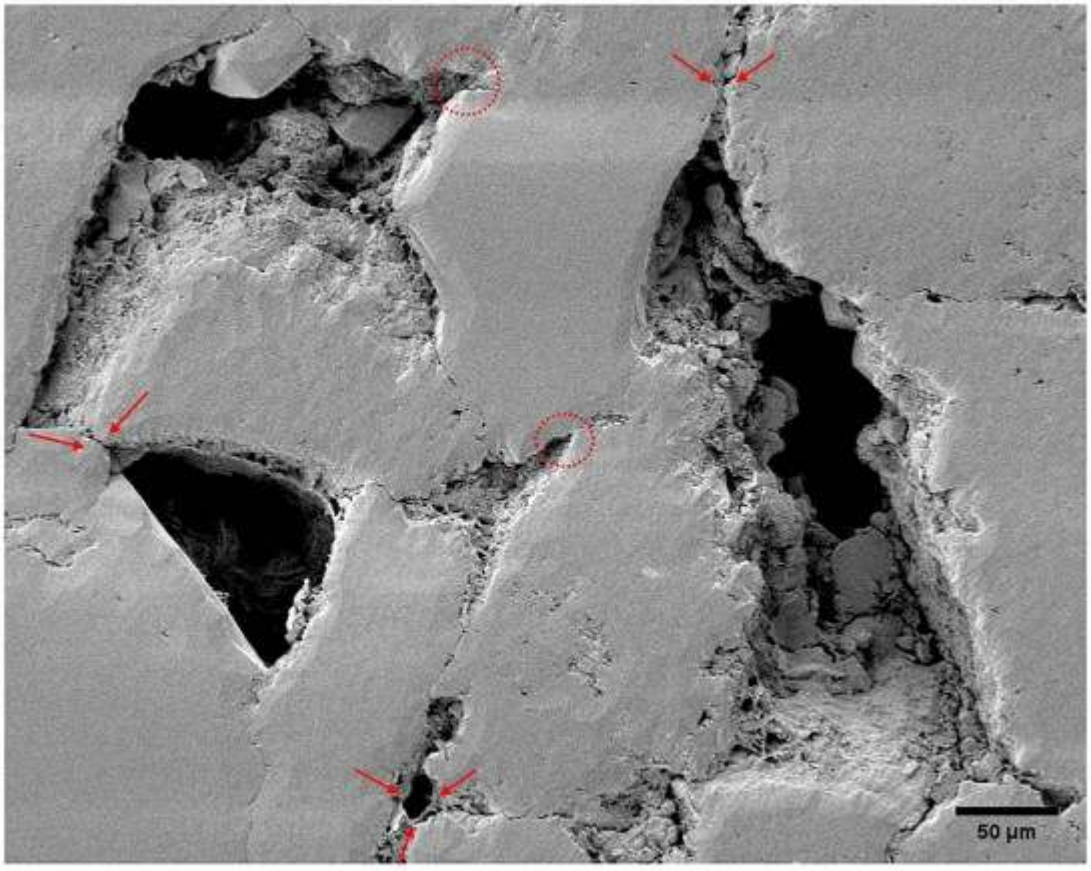

Figure 2. Pore-throat characteristics of the tight sandstone sample.

We measure the pore and throat parameters in the natural rock using rate-controlled mercury intrusion (Padhy et al., 2007; Wang et al., 2018; Yuan &

Swanson, 1989; Zhao et al., 2015, 2019). We use an ASPE 730 rate-controlled mercury intrusion instrument manufactured by US Coretest, a mercury-injection pressure of 0–1,000 psi (about 7 MPa) and a mercury-penetration speed of 0.00005 ml/min. We use values of the contact angle of 140° and interfacial tension of 0.485 N/m to determine pore parameters. The connected porosity is measured using a conventional gas measurement with nitrogen.

We calculate the pore and throat parameters of the digital rocks with the maximum ball algorithm (Al-Kharusi & Blunt, 2007; Dong & Blunt, 2009; Silin et al., 2004). The porosity of digital rocks is computed by counting pixels in the binary images, and the connected pore volume excludes isolated pores.

Because the sample contains a range of pore sizes —large pores connected by small throats—we integrate imaging at two different scales. Macropores are imaged with CT scanning using an UltraXRM-L200 CT scanner. We image a cylinder approximately 1.0 cm in diameter and 1.1 cm in length, with porosity 10.58%, and gas permeability 2.24×10^{-16} m^2. The resolution of CT imaging is 10 μm/pixel, chosen to capture the vast majority of pores. Using contrast enhancement, median filtering, and binarization segmentation, 1,054 CT grayscale images are reconstructed (Figure S1 in the supporting information). To characterize smaller pores, the same sample is resampled into three smaller cylinders approximately 0.2 cm in diameter and 0.2 cm in length and imaged using a FIB-SEM. The images are acquired at the coincident point of SEM and FIB beams, with a resolution of 0.5 μm/pixel (Figure S2), chosen to identify most of the throats and details of pores less than 10 μm.

Figure 3a shows a series of example binary images containing micropores. The same image processing procedure used for the CT images is used to create 82 binary SEM images. An additional 200 subimages of microstructures are extracted from the 82 binary SEM images (examples are shown in Figure 3b), specifically focusing on regions where large pores are associated with smaller pores and cracks. The large structures can be captured by both CT and SEM, allowing us to match macropores at both scales.

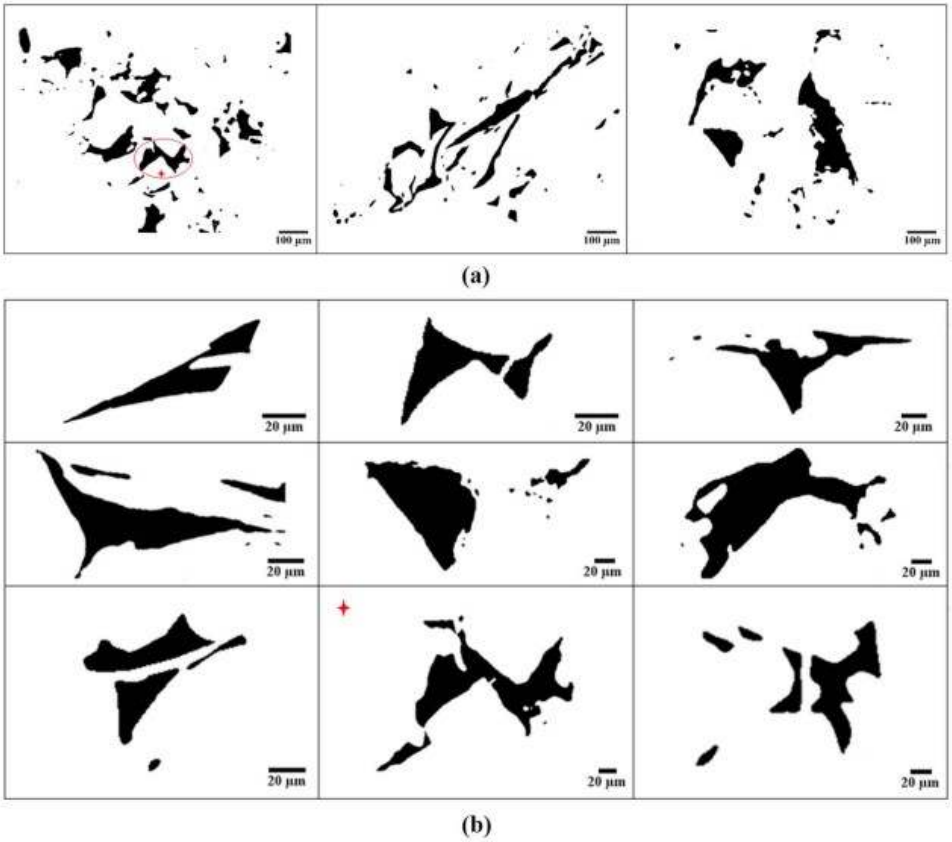

Figure 3. Examples of the scanning electron microscope (SEM) images and subimages (white is solid, and black is pore space), and an example of corresponding relationship between template and SEM image is indicated by a red cross symbol. (a) Subset of the 82 binary SEM images containing micropores, and the size of each presented image stitched together from four SEM images is 2,048 × 1,536 pixels. (b) Subset of the 200 subimages with microstructures extracted from 82 binary SEM images that make up the template library.

3 Multiscale Reconstruction Method

Due to the low resolution of CT images, much of the microstructure is not captured. To overcome the trade-offs between resolution (needed to capture large pore structures) and size (large enough to be representative), we use a template-matching algorithm and superposition to improve the accuracy of CT images with the higher-resolution FIB-SEM images.

3.1 Template-Matching Algorithm

Templates are defined as local structures selected from high-resolution SEM images (Figure 3b). Typically, templates are regions containing smaller structures only seen in the high-resolution images. Each template is chosen to be representative of a type of structure seen or expected in the porous material. Together they form a template library. Template matching is a method to find a specific area in a coarse-scale image that bears statistical resemblance with the template that is being matched. The template is moved through every possible position in the image to identify whether the template resembles the target. When the correlation coefficient R reaches the preset threshold R_0, it is considered to be a match and is recorded. The

matching process is illustrated in Figure 4 and can be summarized in the following steps.

Step 1:

Pixel refinement: The resolution of the template and coarse image need to be identical. The coarse images are thus mapped on to a finer resolution so that the high-resolution and coarse-resolution images have the same pixel size. According to the resolution ratio Ψ of the coarse-resolution image (i.e., matching image) to the high-resolution image (i.e., template), the pixels in the coarse-resolution image are divided into Ψ × Ψ pixels, where black shows void pixels and white shows solid pixels (Figure 4a).

Step 2:

Template matching: For a template T with width w pixels and height h pixels, we consider a matching image I with width W pixels and height H pixels, where, $W > w$ and $H > h$. The number of search steps is $(W - w + 1) \times (H - h + 1)$, and the search range is $1 \le j \le W - w$, $1 \le i \le H - h$; S_{ij} is a target region of the image I in a search step (Figure 4b). Based on correlation analysis (Aitchison & Greenacre, 2002; Chen et al., 2018; Reimann et al., 2017), the similarity D between the two images can be obtained by

$$D(i,j) = \sum_{m=1}^{w}\sum_{n=1}^{h}\left[S_{ij}(m,n) - T(m,n)\right]^2. \quad (1)$$

After normalizing (1), the correlation coefficient R is

$$R(i,j) = \frac{\sum_{m=1}^{w}\sum_{n=1}^{h}\left[S_{ij}(m,n) \times T(m,n)\right]}{\sqrt{\sum_{m=1}^{w}\sum_{n=1}^{h}\left[S_{ij}(m,n)\right]^2}\sqrt{\sum_{m=1}^{w}\sum_{n=1}^{h}\left[T(m,n)\right]^2}}. \quad (2)$$

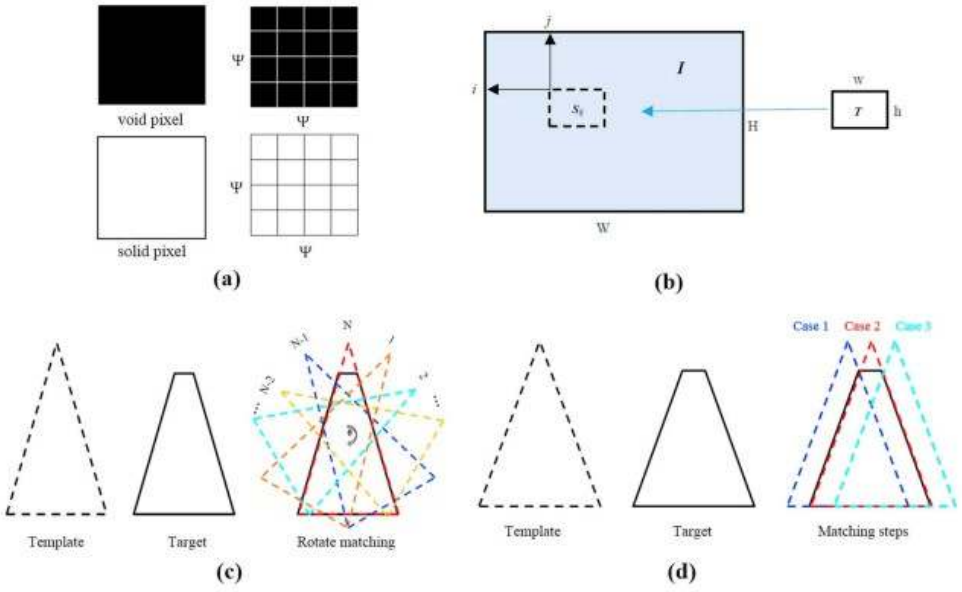

Figure 4. Schematic diagram of template matching principle. (a) Pixel refinement. (b) Template matching process. (c) Rotation matching. (d) Interrelated matches.

Step 3:

Rotation matching: To account for rotations of templates, in each search step, the template is rotated clockwise $N - 1$ times around its center by an angle θ to realize N possible matching angles ($N \times \theta = 360°$), and only the match with the largest correlation coefficient R' ($R' \geq R_0$; R_0 is the preset threshold) is recorded (Figure 4c). If the template is identical to the target, the correlation coefficient $R\ (i, j) = 1$.

Step 4:

Interrelated matches: Interrelated matches are the occurrence of multiple matches on the same target in matching steps. For the interrelated matches, only the match with the largest correlation coefficient is archived. For instance, even if Match 1 ($R_1 \geq R_0$), Match 2 ($R_2 \geq R_0$), and Match 3 ($R_3 \geq R_0$) occur at the same time, only Match 2 is retained because $R_2 > R_1$ and $R_2 > R_3$ (Figure 4d).

3.2 Superposition Principle

The pores of both images are superimposed, and the superimposed pores I_S

$$I_S = I_A \cup I_B, \quad (3)$$

where I_A and I_B represent the pore space of the high-resolution and the coarse-resolution images, respectively. Given that the void and solid pixels of the binary image are characterized by 0 and 1, respectively, the superposition operation is

$$0_A + 0_B = 0_S, 0_A + 1_B = 0_S, 1_A + 0_B = 0_S, 1_A + 1_B = 1_S. \quad (4)$$

We note that by imposing "$1_A + 0_B = 0_S$," the algorithm creates a positive bias for the void pixels, where we assume that the pixels identified as void at low resolution are always void pixels at high resolution. This operation makes the superposition calculation of pores nonattenuating, and the original pore phase is preserved.

3.3 Data Storage

If we define Ψ to be the ratio of the resolution of the coarse- and high-resolution image, the storage of the segmented images will be Ψ^2 times that of the original coarse image. This significant increase in memory storage is undesirable in practice. Here we circumvent this limitation with a strategy to locally improve resolution (Figure 5). In the template-matching process, we only record the coordinates and gray values (0 or 1) of the matched pixels. As shown in Figure 5a, we use (x', y', z', n) to represent a matched pixel in the matching image; here, x' is the abscissa, y' is the ordinate, z' is the number of matching image, n is the gray value after superposition calculation. The original coordinate of matched pixel (x', y', z', n) in the image z' before pixel refinement is ($f(x'/\Psi)$, $f(y'/\Psi)$), where the function f returns the smallest integer greater than or equal to its input (Figure 5b). We can thus find the voxel ($f(x'/\Psi)$, $f(y'/\Psi)$, z') associated with the matched pixel (x', y', z', n) in the 3-D model that is constructed with the raw CT images (Figure 5c). We then divide the voxel ($f(x'/\Psi)$, $f(y'/\Psi)$, z') into $\Psi \times \Psi$

subvoxels; the new coordinate of the subvoxel corresponding to the matched pixel is ($g(x'/\Psi) + h(x'/\Psi)/\Psi$, $g(y'/\Psi) + h(y'/\Psi)/\Psi$, z'), where the function g returns the maximum integer less than or equal to its input and the function h returns the remainder of the division (Figure 5d). At this stage, we assign the gray value of the matched pixel n to the subvoxel ($g(x'/\Psi) + h(x'/\Psi)/\Psi$, $g(y'/\Psi) + h(y'/\Psi)/\Psi$, z'). In this way, we can build a multiresolution 3-D digital rock, while avoiding the massive increase of data.

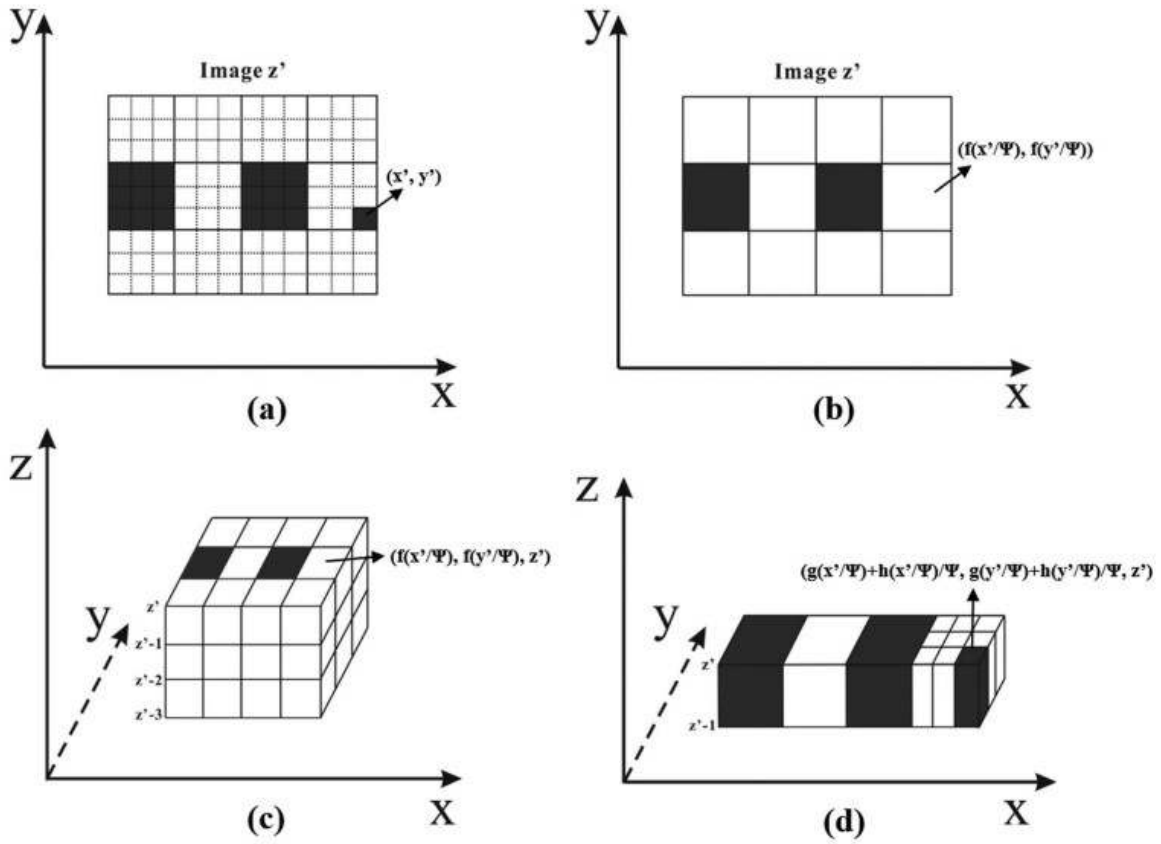

Figure 5. Sketch map of local resolution improvement; black is pore (the gray value is 0), and white is solid (the gray value is 1). (a) A matched pixel (x', y', z', n) in the matching image z'. (b) The original coordinate of matched pixel (x', y', z', n) in the image z' before pixel refinement. (c) The coordinate of the voxel associated with the matched pixel (x', y', z', n) in the computed tomography-only digital rock. (d) The coordinate of the voxel associated with the matched pixel (x', y', z', n) in the coupled computed tomography-scanning electron microscope digital rock.

4 Results and Validation

Using the template-matching algorithm and superposition principle, we searched for 50, 100, 150, and 200 subimage templates in 1,054 CT images, where we choose $R_0 = 0.95$, $\theta = 5°$, $N = 72$, $\Psi = 20$. We identify 576, 1,560, 2,331, and 2,834 matches, respectively. The calculated connected porosity of the four sets of coupled CT-SEM images and raw CT images are shown in Figure 6. We find that the connected porosity of the coupled CT-SEM image group increases with increasing number of templates and is higher than that of the raw CT image (7.37%). When the number of templates reaches 200, the connected porosity of the coupled CT-SEM images is similar to the measured porosity of the real rock (10.58%). In this case, the maximum

number of matches for a single template is 37, the minimum number is 1, and the mode is 12 (Figure 7a). For a single CT image, the maximum number of matches is 8, the minimum number is 0, and the mode is 2 (Figure 7b). The existence of template matches implies that the microstructures imaged at high resolution are indeed embedded in the CT images. The occurrence of multiple matches of the same template implies that the rock develops similar microstructures throughout its volume during depositional and diagenetic processes.

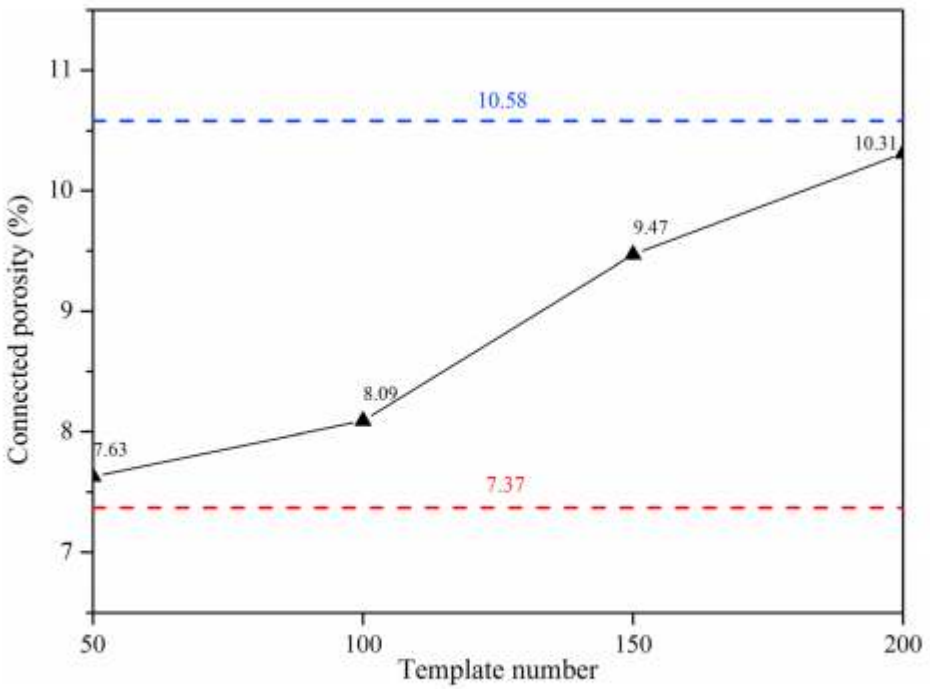

Figure 6. The relationship between the connected porosity of coupled computed tomography-scanning electron microscope image groups and the number of templates; the red dashed line denotes the connected porosity of the raw computed tomography images, and the blue dashed line denotes the measured porosity of the real rock.

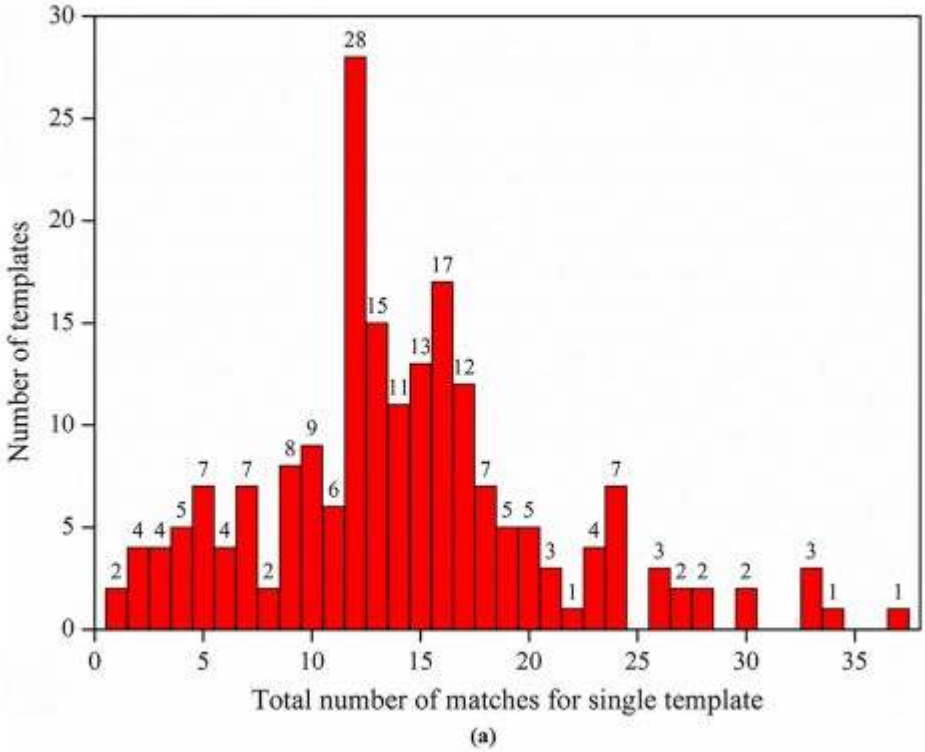

Figure 7. (a) Number distribution histogram of templates corresponding to the number of different matches for a single template. (b) Number distribution sector diagram showing the number of template matches in each computed tomography image.

To validate the method, we first compare features of the pore space in the real rock with the digital versions. We use 1,054 raw CT images coupled with

200 templates to construct 3-D digital rocks. From Figure 8, we can see that the number of micropores in the new digital rock increases. From Table 1, we can see that the number of pores in the digital rock is similar to that in the real rock. This is because the pore size is often large and most of the pores can also be identified in coarse-resolution images. However, the coarse resolution also leads to the omission of a large number of throats, and as a result the number of throats of the CT-only digital rock is much lower than that of the new digital rock. As a consequence, the average coordination number of the CT-only digital rock is lower than that of the new digital rock, and the pore connectivity is underestimated. The porosity of the new digital rock is 21.14% higher than that of the CT-only digital rock due to the embedded microstructures. In fact, the porosity of the new digital rock is slightly higher than the connected porosity of the real rock owing to the existence of isolated pores and throats. Because of the absence of micropores and throats, the connected porosity of the CT-only digital rock is distinctly smaller than that of real rock and new digital rock. We compare the pore and throat radius distribution of digital rocks with that of the real rock. Figure 9a shows that the pore radius of the real rock ranges from 50 μm to 220 μm, with a dominant radius of 107 μm; the pore radius of the new digital rock has a broader range from 30 to 234 μm with dominant radius of 102 μm; the pore radius of the CT-only digital rock has a more narrow distribution, from 80 to 200 μm and dominant radius of 120 μm. There is no significant difference between the pore radius distribution of digital rocks and that of real rock, but the pore radius distribution of new digital rock is closer to that of real rock. From Figure 9b, we can see that there is a distinct difference in the distribution of throat radius between the CT-only digital rock, the real rock, and the new digital rock. Since the coarse resolution of CT images is 10 μm, the throat radius of the CT-only digital rock is distributed from 10 to 40 μm, the dominant radius of throats is 20 μm. However, the throat radius of the real rock ranges from 0.4 to 2.2 μm, and the dominant radius of throats is 0.9 μm; the throat radius of the new digital rock ranges from 0.5 to 10 μm, and the dominant radius of throats is 1.0 μm. We find that the distribution of throat radius of the new digital rock is consistent with that of the real rock. The macroscale imaging is thus able to capture the pores but not the throats whose dimensions are in general smaller than the CT image resolution; however, the template matching allows us to recover the smaller-scale throats.

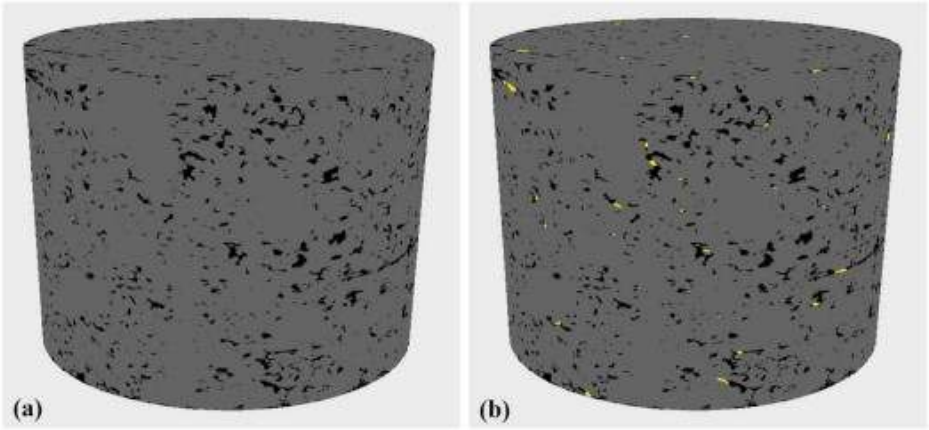

Figure 8. (a) Computed tomography (CT)-only digital rock constructed with raw CT images; black is pore space, and gray is solid. (b) New digital rock constructed by the CT images coupled with 200 templates; black is pore space, gray is solid, and yellow is the new pore space.

Table 1
Petrophysical Parameters of the Real Rock and the Digital Rocks

Parameters	Real rock	CT-only digital rock	Error %	New digital rock	Error %
Porosity	—	8.94%	—	10.83%	—
Connected porosity	10.58%	7.37%	30.34	10.31%	2.55
Pore number	1,320	1,229	6.89	1,336	1.21
Throat number	—	1,635	—	2,145	—
Average coordination number	—	2.88	—	3.25	—
Permeability (m^2)	2.24×10^{-16}	1.09×10^{-13}	—	3.12×10^{-15}	—

Note. CT = computed tomography. Porosity = (pore volume/rock volume)*100%; connected porosity = (connected pore volume/rock volume)*100%. The coordination number describes the number of throats connected to the single pore; the larger the coordination number, the better the pore connectivity.

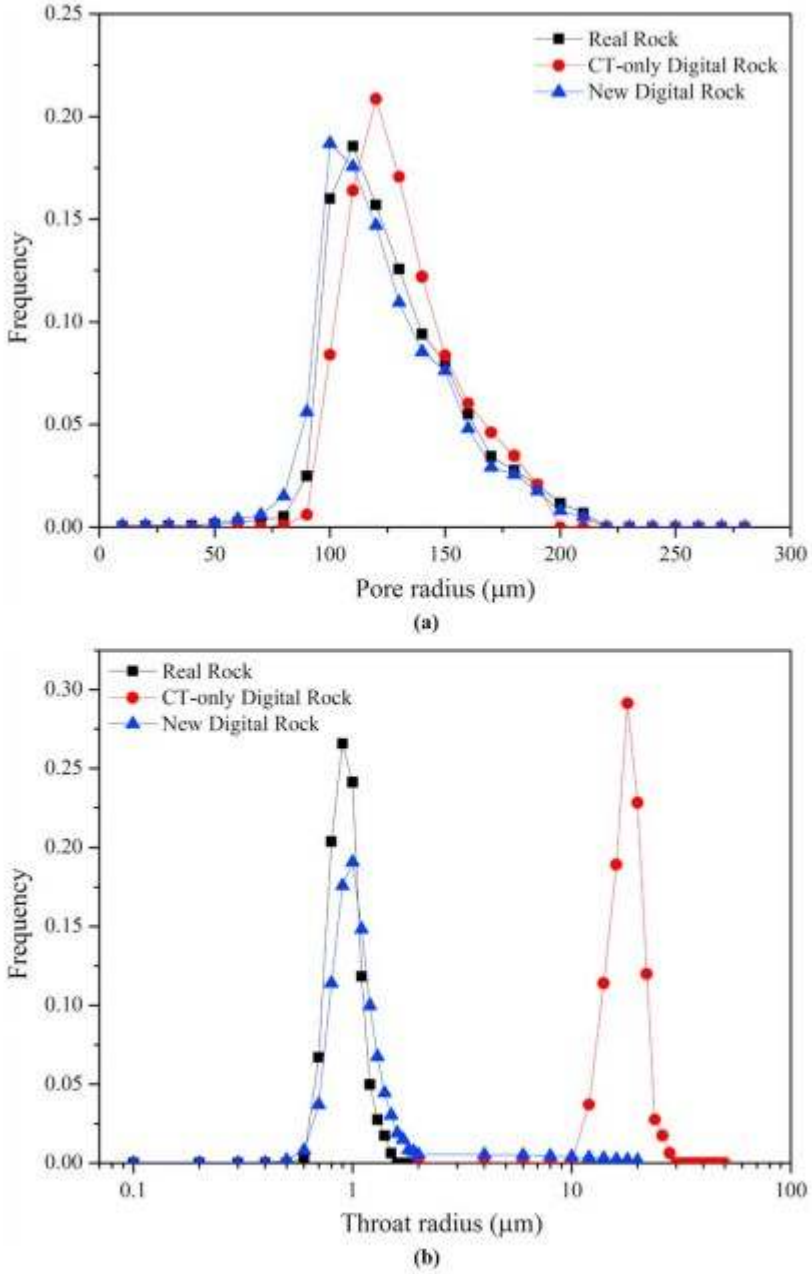

Figure 9. Pore and throat radius distribution of digital rocks and the real rock. (a) Comparison of pore radius distribution between digital rocks and the real rock. (b) Comparison of throat radius distribution between digital rocks and the real rock. CT = computed tomography.

Ideally, we could also estimate permeability as a second validation. Unfortunately, neither the original CT-only nor the new digital rocks contain a connected network of pores spanning the sample, and thus, the computed permeability would be zero. Permeability can, however, be computed for subvolumes. In order to use a gridded model to compute permeability, given a mean pore throat size of about 1 micron, we would need a spatial

resolution of at least 0.2 microns to resolve flow (e.g., Bakhshian et al., 2018). While lattice Boltzmann methods scale well in parallel, to simulate our imaged volume requires a domain 50,000 × 50,000 × 50,000, which greatly exceeds our group's present computing capabilities. We thus assess permeability on subvolumes with a pore network model (PNM; Blunt, 2001; Siena et al., 2014; Xiong et al., 2016). Compared to lattice Boltzmann methods, PNMs require much less computing time and memory due to the inherent simplifications of void space. We further choose a representative elementary volume as the smallest subset of the pore space that shows similar volume-averaged properties (here the porosity) as larger subsets (García-Salaberri et al., 2018). We cut 3-D subvolumes with linear dimensions ranging from 0.5 to 7 mm from the center of the digital rock and compute the porosity of these subvolumes. As shown in Figure S3, when the dimension reaches 4 mm, the porosities of the subvolumes extracted from the CT-only digital rock and the new digital rock tend to be stable. Therefore, the representative elementary volumes of the digital rocks are determined to be 4 × 4 × 4 mm (Figure S4). Since porous flow occurs in the connected pores, we extract the largest connected pore network for each digital rock (Figure S5) and generate the PNMs (Figure S6) for permeability prediction. As shown in Figure S6, the connected pore network of the new digital rock is larger in spatial extent than that of the CT-only digital rock, and more isolated pores are connected by small pore-throats. The absolute permeabilities parallel to the core of the two PNMs are listed in Table 1. The simulated results show that the permeability of the new digital rock is 2 orders of magnitude lower than that of the CT-only digital rock due to the addition of small pore-throats to the new digital rock. Both computed permeabilities exceed the experimental permeability, owing to the absence of smaller pore-throats, less than 0.5 microns, that allow connected networks to extend over much larger scales. Accurately capturing pore throat size in these tight rocks is critical to computing permeability. The permeability of the new digital rock is within an order of magnitude of experimental measured permeability, whereas the CT-only digital rock permeability was 3 orders of magnitude too large.

The template-matching approach restores some corner structures of macropores, micropores, and fine throats, as identified in Figure 2, void spaces that cannot be identified at coarse resolution (10 μm per pixels). Overall, the new digital rock shows good agreement with the natural rock with respect to geometric statistics of the pore structure.

5 Summary and Future Directions

We put forward the concept of template matching for the construction of multiscale digital rocks in order to address the trade-off between imaging resolution and sample size. By expanding the resolution of 2-D images, we can create a higher-resolution 3-D model. The microstructures in the natural rock are selected as templates for those assumed to be embedded in the coarse-resolution images. This approach is empirical in that it is based on

correlations seen at different scales and implicitly assumes that the microstructures have a physical origin so that they are repeated. However, the approach does not need to make assumptions about self-similarity or statistical properties of the pore space. Provided the number of templates is large enough and sample from a large enough region of the rock, the approach should also account for heterogeneity of the rock.

There are three future directions. First, we only implemented two-level matching, but the approach should be generalized to multiple scales, for example, to connect centimeter-millimeter-micron-nanometer scales. Second, template matching with 3-D templates, while computationally much more expensive to implement (correlations must be computed in three directions and two angular rotations), should be more accurate at recognizing microstructure but might also require fewer templates. Third, it may be possible to use differential imaging of CT scans (by saturating pores with a high-contrast fluid) to validate at least some aspects of the imaging improvement by providing some additional constraints on subresolution structures (e.g., Lin et al., 2016).

Acknowledgments

We gratefully acknowledge financial support from the National Science and Technology Major Project of China (2017ZX05013-001 and 2017ZX05069-003), the Miller Institute for Basic Research in Science (X. F.), and NSF 1724469 (M. M.); thank China Scholarship Council for funding Wei Lin's visiting study at University of California Berkeley; and are also grateful to Petrochina Company Limited for providing the software “Multi-scale 3D reconstruction and dynamic simulation system of tight reservoir digital rock” (Registered Copyright No. 2019SR0150745) in this study. The reviewers and editors' comments are highly appreciated. The authors want to thank Senior Engineer Hekun Guo and Dr. Haibo Li from Research Institute of Petroleum Exploration and Development, PetroChina Company Limited, for their technical support in the rate-controlled mercury intrusion experiment and also would like to especially recognize Juan Wang from China Oilfield Services Limited for the expertise and help in data processing. The data used in this paper are deposited in the Baidu Web Drive and can be downloaded at the website https://pan.baidu.com/s/1lQX00KTvy-3vcFdxn6Nq6A (code: noeb).

References

Aitchison, J., & Greenacre, M. (2002). Biplots of compositional data. *Journal of the Royal Statistical Society: Series C: Applied Statistics*, 51(4), 375– 392. https://doi.org/10.1111/1467-9876.00275

Al-Kharusi, A. S., & Blunt, M. J. (2007). Network extraction from sandstone and carbonate pore space images. *Journal of Petroleum Science and Engineering*, 56(4), 219– 231. https://doi.org/10.1016/j.petrol.2006.09.003

Bakhshian, S., Shi, Z. F., Sahimi, M., Tsotsis, T. T., & Jessen, K. (2018). Image-based modeling of gas adsorption and deformation in porous media. *Scientific Reports*, 8(1), 8249. https://doi.org/10.1038/s41598-018-26197-8

Blunt, M. J. (2001). Flow in porous media-pore-network models and multiphase flow. *Current Opinion in Colloid & Interface Science*, 6(3), 197– 207. https://doi.org/10.1016/S1359-0294(01)00084-X

Chen, J., Zhou, D., Lyu, C., & Lu, C. (2018). An integrated method based on CEEMD-SampEn and the correlation analysis algorithm for the fault diagnosis of a gearbox under different working conditions. *Mechanical Systems and Signal Processing*, 113, 102– 111. https://doi.org/10.1016/j.ymssp.2017.08.010

Dong, H., & Blunt, M. J. (2009). Pore-network extraction from micro-computerized-tomography images. *Physical Review E*, 80(3), 036307. https://doi.org/10.1103/PhysRevE.80.036307

García-Salaberri, P. A., Zenyuk, I. V., Shum, A. D., Hwang, G., Vera, M., Weber, A. Z., & Gostick, J. T. (2018). Analysis of representative elementary volume and through-plane regional characteristics of carbon-fiber papers: Diffusivity, permeability and electrical/thermal conductivity. *International Journal of Heat and Mass Transfer*, 127(Part B), 687– 703. https://doi.org/10.1016/j.ijheatmasstransfer.2018.07.030

Hwa, L. C., Rajoo, S., Noor, A. M., Ahmad, N., & Uday, M. B. (2017). Recent advances in 3D printing of porous ceramics: A review. *Current Opinion in Solid State & Materials Science*, 21(6), 323– 347. https://doi.org/10.1016/j.cossms.2017.08.002

Ishutov, S., Jobe, T. D., Zhang, S., Gonzalez, M., Agar, S. M., Hasiuk, F. J., Watson, F., Geiger, S., Mackay, E., & Chalaturnyk, R. (2018). Three-dimensional printing for geoscience: Fundamental research, education, and applications for the petroleum industry. *AAPG Bulletin*, 102(1), 1– 26. https://doi.org/10.1306/0329171621117056

Jiang, Q., Feng, X., Song, L., Gong, Y., Zheng, H., & Cui, J. (2016). Modeling rock specimens through 3D printing: Tentative experiments and prospects. *Acta Mech. Sin.*, 32(1), 101– 111. https://doi.org/10.1007/s10409-015-0524-4

Lin, Q., Al-Khulaifi, Y., Blunt, M. J., & Bijeljic, B. (2016). Quantification of sub-resolution porosity in carbonate rocks by applying high-salinity contrast brine using X-ray microtomography differential imaging. *Advances in Water Resources*, 96, 306– 322. https://doi.org/10.1016/j.advwatres.2016.08.002

Ma, L., Fauchille, A. L., Dowey, P. J., Pilz, F. F., Courtois, L., Taylor, K. G., & Lee, P. D. (2017). Correlative multi-scale imaging of shales: A review and future perspectives. *Geological Society Special Publication, London*, 454(1), 175– 199. https://doi.org/10.1144/SP454.11

Padhy, G. S., Lemaire, C., Amirtharaj, E. S., & Ioannidis, M. A. (2007). Pore size distribution in multiscale porous media as revealed by DDIF-NMR, mercury porosimetry and statistical image analysis. *Colloids and Surfaces A: Physicochemical and Engineering Aspects*, 300(1-2), 222– 234. https://doi.org/10.1016/j.colsurfa.2006.12.039

Reimann, C., Filzmoser, P., Hron, K., Kynclova, P., & Garrett, R. G. (2017). A new method for correlation analysis of compositional (environmental) data-a worked example. *The Science of the Total Environment*, 607-608, 965– 971. https://doi.org/10.1016/j.scitotenv.2017.06.063

Siena, M., Riva, M., Hyman, J. D., Winter, C. L., & Guadagnini, A. (2014). Relationship between pore size and velocity probability distributions in stochastically generated porous media. *Physical Review E*, 89(1), 013018. https://doi.org/10.1103/PhysRevE.89.013018

Silin, D. B., Jin, G. D., & Patzek, T. W. (2004). Robust determination of the pore-space morphology in sedimentary rocks. *Journal of Petroleum Technology*, 56(5), 69– 70. https://doi.org/10.2523/84296-ms

Sok, R. M., Varslot, T., Ghous, A., Latham, S., Sheppard, A. P., & Sheppard, M. A. (2010). Pore scale characterization of carbonates at multiple scales: Integration of Micro-CT, BSEM, and FIBSEM. *Petrophysics*, 51, 379– 387. https://www.onepetro.org/journal-paper/SPWLA-2010-v51n6a1

Wang, L., Wang, S., Zhang, R., Wang, C., Xiong, Y., Zheng, X., Li, S., Jin, K., & Rui, Z. (2017). Review of multi-scale and multi-physical simulation technologies for shale and tight gas reservoirs. *Journal of Natural Gas Science and Engineering*, 37, 560– 578. https://doi.org/10.1016/j.jngse.2016.11.051

Wang, X., Hou, J., Song, S., Wang, D., Gong, L., Ma, K., Liu, Y., Li, Y., & Yan, L. (2018). Combining pressure-controlled porosimetry and rate-controlled porosimetry to investigate the fractal characteristics of full-range pores in tight oil reservoirs. *Journal of Petroleum Science and Engineering*, 171, 353– 361. https://doi.org/10.1016/j.petrol.2018.07.050

Wu, T., Li, X., Zhao, J., & Zhang, D. (2017). Mutiscale pore structure and its effect on gas transport in organic-rich shale. *Water Resources Research*, 53, 5438– 5450. https://doi.org/10.1002/2017WR020780

Xiong, Q., Baychev, T. G., & Jivkov, A. P. (2016). Review of pore network modelling of porous media: Experimental characterisations, network constructions and applications to reactive transport. *Journal of Contaminant Hydrology*, 192, 101– 117. https://doi.org/10.1016/j.jconhyd.2016.07.002

Yuan, H. H., & Swanson, B. F. (1989). Resolving pore-space characteristics by rate-controlled porosimetry. *SPE Formation Evaluation*, 4(1), 17– 24. https://doi.org/10.2118/14892-PA

Zhao, H., Ning, Z., Wang, Q., Zhang, R., Zhao, T., Zhao, T., Niu, T., & Zeng, Y. (2015). Petrophysical characterization of tight oil reservoirs using pressure-

controlled porosimetry combined with rate-controlled porosimetry. *Fuel*, 154, 233– 242. https://doi.org/10.1016/j.fuel.2015.03.085

Zhao, X., Yang, Z., Lin, W., Xiong, S., Luo, Y., Wang, Z., Chen, T., Xia, D., & Wu, Z. (2019). Study on pore structures of tight sandstone reservoirs based on nitrogen adsorption, high-pressure mercury intrusion, and rate-controlled mercury intrusion. *Journal of Energy Resources Technology-ASME*, 16(11), 675– 684. https://doi.org/10.115/1.4043695